

*Work supported in part by the National Science Foundation, and also by the Oregon State University Research Council and Computer Center.

†Now at the Naval Weapons Laboratory, Dahlgren, Virginia 22248.

‡Deceased.

§Now at Walla Walla College, College Place, Washington 99324.

|| Now at University of Maryland, College Park, Maryland 20742.

¹G. Burgun, J. Meyers, E. Pauli, B. Tallini, J. Vrana, A. DeBellefon, A. Berthon, K. L. Rangan, J. Beaney,

S. M. Deen, C. M. Fisher, and J. R. Smith, Nucl. Phys. B8, 447 (1968).

²P. M. Dauber, J. P. Berge, J. R. Hubbard, D. W. Merrill, and Richard A. Muller, Phys. Rev. 179, 1262 (1969).

³G. M. Bingham, V. Cook, J. W. Humphrey, O. R. Sander, R. W. Williams, G. E. Masek, T. Maung, and H. Ruderman, Phys. Rev. D 1, 3010 (1970).

⁴N. D. Sossong, R. Ellsworth, J. R. Carlson, H. F. Davis, and D. E. Jauch, Phys. Rev. D 5, 2711 (1972).

⁵J. R. Carlson, Ph.D. thesis, Oregon State University, 1970 (unpublished).

PHYSICAL REVIEW D

VOLUME 7, NUMBER 9

1 MAY 1973

Reactions $K^-d \rightarrow \bar{K}^0\pi^-d$ and $K^-d \rightarrow \bar{K}^0\pi^-np_s$ at 5.5 GeV/c†

D. Johnson,* Y. Cho, M. Derrick, B. Musgrave, and T. Wangler
Argonne National Laboratory, Argonne, Illinois 60439

R. Ammar,‡ R. Davis, W. Kropac, and H. Yarger
University of Kansas, Lawrence, Kansas 66044

G. C. Fox

Lauritsen Laboratory of Physics, California Institute of Technology, Pasadena, California 91109

(Received 11 August 1972)

New data are presented on cross sections and angular distributions of resonances produced in the reactions $K^-d \rightarrow \bar{K}^0\pi^-d$ and $K^-d \rightarrow \bar{K}^0\pi^-np_s$ at 5.5 GeV/c. The production mechanisms and decay angular distributions are analyzed for the $\bar{K}^*(890)$, $\bar{K}^*(1420)$, and $\Delta(1236)$ resonances. The $\bar{K}^0\pi^-np_s$ final state is discussed in terms of the Veneziano B_5 model and also using the Van Hove longitudinal-phase-space technique. In addition, a Regge model with absorption is used to describe $\Delta(1236)$ production in the reaction $\bar{K}N \rightarrow \bar{K}\Delta(1236)$. The spherical harmonic moments of the $\bar{K}^0\pi^-$ system as a function of $K\pi$ mass are discussed for the reaction $K^-d \rightarrow \bar{K}^0\pi^-p + MM$.

I. INTRODUCTION

We present here a study of resonance production in the reactions

$$K^-d \rightarrow \bar{K}^0\pi^-np, \quad (1.1)$$

$$K^-d \rightarrow \bar{K}^0\pi^-d, \quad (1.2)$$

$$K^-d \rightarrow \bar{K}^0\pi^-p + MM, \quad (1.3)$$

where the \bar{K}^0 meson decays into charged pions. These results come from an analysis of 370 000 pictures taken with the 30-in. deuterium bubble chamber. The chamber was exposed to an electrostatically separated, high-purity¹ beam of 5.5-GeV/c K^- mesons produced at the Zero Gradient Synchrotron. Some results from this exposure have already been published.²

Previous studies of K^- -deuterium interactions

over a wide range of momenta have shown that coherent production of the $\bar{K}^{*0}(890)$ and $\bar{K}^{*0}(1420)$ are dominant features of reaction (1.2). The deuteron form factor ensures that \bar{K}^* production occurs for only very small momentum transfers, and the \bar{K}^* production is expected to be mediated through $I=0$ (ω^0) t -channel exchange. The interest in studying reaction (1.1) lies in the possibility of observing K^-n interactions. It is generally observed that the fractions of $\bar{K}^*(890)$ and $\Delta(1236)$ production contributing to the $K\pi N$ final state as well as the production and decay properties of the $\bar{K}^{*0}(890)$ are roughly independent of the bombarding K^- energy in the range 3–5 GeV/c. This is also true of the reaction $K^+p \rightarrow K^0\pi^+p$ up to 10 GeV/c.³ We present data on the production and decay processes for these resonances at 5.5 GeV/c and compare our results to the predictions of some models.

TABLE I. Cross sections for $K^-d \rightarrow \bar{K}^0\pi^-d$.

No. observed events in final state $\bar{K}^0\pi^-d$	Cross section $K^-d \rightarrow \bar{K}^0\pi^-d$	Cross section ^a $K^-d \rightarrow \bar{K}^{*-}(890)d$
72	$63 \pm 16 \mu\text{b}$	$69 \pm 20 \mu\text{b}$

^a The cross section is for all decay modes of the $\bar{K}^{*-}(890)$.

II. EXPERIMENTAL DETAILS

A. Event Collection

The results presented here come from measurement of events having one or two outgoing tracks plus an associated visible V decay. In the case of events having two charged particles plus a V , the positive track was required to stop in the chamber and to have an ionization density consistent with being either a proton or a deuteron. The scanning efficiency was measured by a double scan made on 30% of the film.

Events found in the scanning were measured either on conventional image-plane digitizers or on the POLLY device.⁴ The events measured using conventional machines⁵ consisted of those not suitable for automatic measurement due to insufficient spatial separation between the beam tracks and in addition the remeasurements from the sample initially measured on POLLY.

Geometric reconstruction and kinematic fitting of the events was done by Argonne versions of the TVGP and GRIND programs.⁶ Events failing geometric reconstruction for any reason were remeasured once. After the kinematic fitting, events were visually checked for consistency between actual track ionization density and that predicted by the kinematic fit where necessary.

Corrections were applied for losses in the scanning and measuring phases of the experiment in producing the cross sections given in Tables I and II. Corrections have also been made for χ^2 probability cuts, \bar{K}^0 escape loss, and undetected \bar{K}^0 decay modes. In the case of reaction (1.1), a correction was also made for the Glauber screening effect and for the proton spectator momentum cut applied. The cross sections presented are based on the total K^- beam track length in the fiducial region estimated by a beam track count every 20th frame. These factors and also the assignment of events to reactions (1.1)–(1.3) are discussed in the following sections.

B. Separation of the Coherent and Breakup Events

It is to be expected that events fitting the four-constraint hypothesis (1.2) would also satisfy the one-constraint hypothesis (1.1) in which the deuteron is broken up. Events showing such ambiguity are those having the proton and neutron closely collinear with small relative momentum. Figure 1(a) shows the distribution in $\cos\theta_{pn}$, the angle between proton and neutron directions, for all events fitting hypothesis (1.1). Events that also fit the deuteron hypothesis (1.2) appear shaded in this figure and demonstrate the expected strong tendency for collinearity between the neutron and proton. Conversely, the unshaded events have an approximately isotropic distribution in $\cos\theta_{pn}$.

In addition, the range-energy relation for stopping protons and deuterons helps resolve the proton-deuteron ambiguity. An event from reaction (1.2) will satisfy the kinematics of reaction (1.1) with the ratio $|p_n|/|p_p| \approx 0.68$ for the neutron and proton momenta, provided the deuteron stops.⁷

TABLE II. Cross section for $K^-d \rightarrow \bar{K}^0\pi^-np_s$ and resonance cross sections for $\bar{K}^0\pi^-n(p_s)$ final state.

Reaction	No. of events		$K^-d \rightarrow \bar{K}^0\pi^-np_s$ Cross section (μb) ^a	
	471	Dalitz-plot fit resonant fractions	No. of events	Resonance cross section (μb)
$K^-n \rightarrow \bar{K}^{*-}(890)n$ \downarrow $K^0\pi^-$		$(27.4 \pm 2.6)\%$	111	116 ± 19^b
$K^-n \rightarrow \bar{K}^{*-}(1420)n$ \downarrow $\bar{K}^0\pi^-$		$(6.6 \pm 2.1)\%$...	28 ± 5
$K^-n \rightarrow \bar{K}^0\Delta^-(1236)$		$(27.3 \pm 2.7)\%$	123	116 ± 19

^a This estimate is corrected for background and includes further corrections for Glauber shadow effect (1.06), χ^2 -probability cut (1.04), spectator momentum cut (1.03), and unseen K_1^0 decay mode.

^b The cross section for $K^-n \rightarrow \bar{K}^{*-}(890)n$ corrected for all decay modes of the $\bar{K}^{*-}(890)$ is $177 \pm 29 \mu\text{b}$.

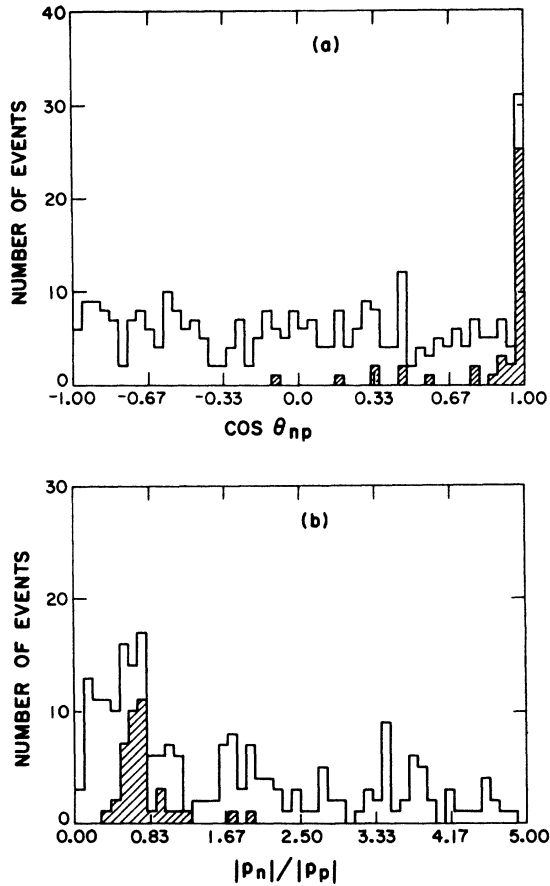


FIG. 1. (a) The angle between the neutron and proton directions and (b) the ratio of the magnitudes of the neutron and proton momenta for events fitting $K^-d \rightarrow \bar{K}^0\pi^-np$. The shaded events also fit $K^-d \rightarrow \bar{K}^0\pi^-d$.

Figure 1(b) shows the distribution in the fitted momentum ratio $|p_n|/|p_p|$ for events having a stopping track and which fit reaction (1.1). Events also fitting reaction hypothesis (1.2) are shown shaded. The clustering of the shaded events about the value 0.68 supports the assignment of these events to reaction (1.2). These effects are summarized in Fig. 2(a) where $\cos\theta_{pn}$ is plotted versus the $|p_n|/|p_p|$ ratio. The clustering of events is interpreted as belonging to genuine deuteron events. For events fitting the $\bar{K}^0\pi^-np$ hypothesis but not the $\bar{K}^0\pi^-d$ hypothesis, the scatter plot in Fig. 2(b) shows no such clustering of events, a good indication that coherent events are not being lost into the breakup channel. The smearing out of the clusters seen in Figs. 1(a) and 1(b) arises primarily from very short stopping tracks, which are often poorly measured. Events with a measured stopping particle which fitted both (1.1) and (1.2) were therefore assigned to the latter if

$$0.2 \leq |p_n|/|p_p| \leq 1.2 \quad (2.1)$$

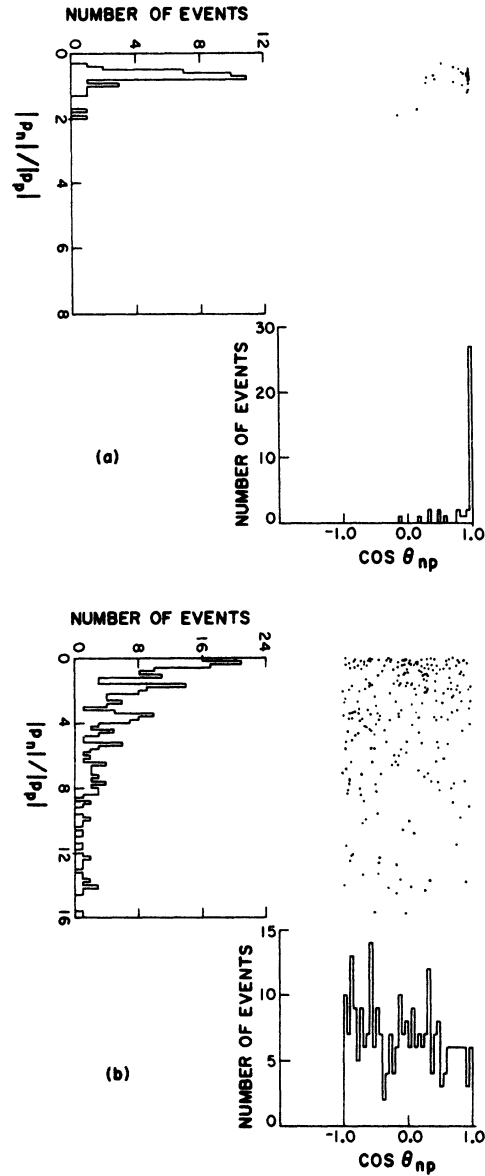


FIG. 2. Data shown in Fig. 1 separated into (a) those events fitting both reactions and (b) those events only fitting $K^-d \rightarrow \bar{K}^0\pi^-pn$.

and

$$\cos\theta_{np} \geq 0.6. \quad (2.2)$$

In Fig. 3, we have plotted the np mass spectrum for events fitting hypothesis (1.1) with an observed stopping proton. Events shown shaded also fit hypothesis (1.2), assuming a stopping deuteron, and the obvious peaking about the mass of the deuteron supports the assignment of these as genuine coherent events. We estimate the loss of coherent events into the breakup events to be less than 10%.

The deuteron will fail to produce a visible track

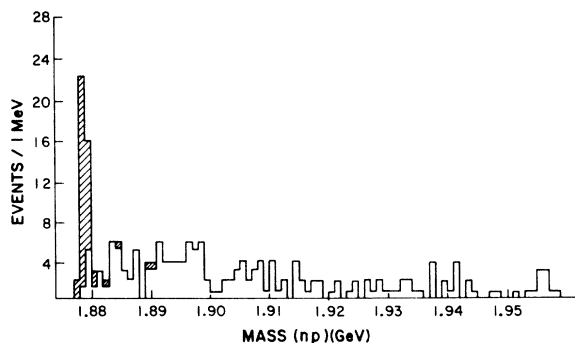
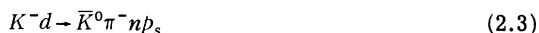


FIG. 3. (np) effective mass for the events of Fig. 1.

if its momentum is smaller than about 130 MeV/c. For reaction (1.2), this corresponds to a squared four-momentum transfer of about $0.02 \text{ (GeV}/c)^2$ in the $\bar{K}^{*}(890)$ mass region. The bias introduced by completely neglecting these events affects only the very forward part of the differential cross section for the reaction $K^-d \rightarrow \bar{K}^{*}(890)d$ and is not severe. In the following analysis, however, we include the small number of events having an unseen deuteron which satisfy hypothesis (1.2). The cross section obtained for reaction (1.2) is given in Table I.

After removing the 4c (4-constraint) events belonging to reaction (1.2), the missing mass for events consistent with reaction (1.1) or (1.3) is shown in Fig. 4. The events which are consistent with the hypothesis (1.1) are shown shaded. The events having an unseen proton track are included in this distribution. For these events, a kinematic fit to (1.1) was obtained by using starting variables $\vec{p} = 0$ with errors $\Delta p_x = \Delta p_y = 0.75 \Delta p_z = 30 \text{ MeV}/c$.⁷ This sample is, of course, enriched with events from the reaction



because of the scanning criteria used. The cross section for reaction (2.3) is estimated from such a missing-mass distribution after drawing a reasonable background under the neutron peak. The resolution in missing mass squared for events with a measured proton track is superior to that for those without, although all events have been included.

For further study of reaction (2.3), we select events with missing mass squared in the range $0.48\text{--}1.16 \text{ GeV}^2$, which includes an estimated 6% background. A further cut is made in terms of the kinematic χ^2 probability. The distribution in this latter quantity for events fitting reaction (1.1) shows a small excess for probabilities less than 4%; hence, we have imposed a minimum-probability requirement of 4% in selecting events of this final state in order to reduce the number of spuri-

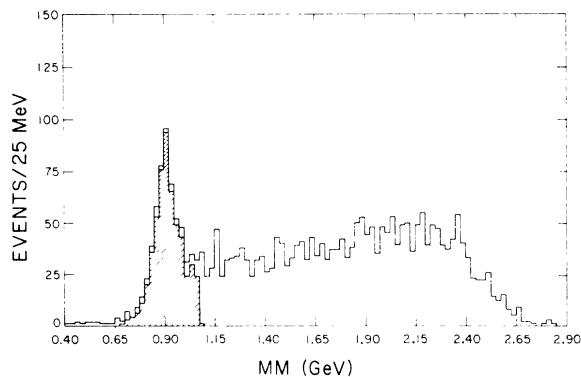


FIG. 4. Missing mass for the events consistent with $K^-d \rightarrow \bar{K}^0 \pi^- p + \text{MM}$. The events fitting $K^-d \rightarrow \bar{K}^0 \pi^- p n$ are shown shaded.

ous fits. This cut is quite strongly correlated with that on the missing mass.

The final selection made is to obtain a sample of neutron-target interactions belonging to (2.3) above. When the final-state proton has insufficient energy to produce a visible track, it is assumed to be the spectator nucleon.⁸ For the remainder of the events, our criterion consists essentially in selecting the slower nucleon as the spectator in the interaction, although we also assume that any nucleon recoiling into the backward hemisphere with respect to the beam direction is a spectator nucleon. This latter assumption is somewhat modified by the Fermi motion of the struck nucleon, but this effect is small and affects less than 10% of the nucleons observed in the backward hemisphere.

To illustrate the momentum-angle correlation for the spectator nucleon, we have plotted in Fig. 5(a) the cosine of the angle between the beam and the proton versus the ratio of the absolute value of the neutron to proton momentum. This is shown for $\bar{K}^0 \pi^- np$ events with visible proton track after removing $\bar{K}^0 \pi^- d$ events. One sees from this distribution that when the momentum ratio falls below about 2, an anisotropy develops in the angular distribution which becomes forward-peaked with respect to the beam. This is a consequence of the inclusion of recoil protons from K^-p interactions.

In Fig. 5(b) the cosine angle between neutron and beam is plotted against this same momentum ratio. Here, isotropy in the angular distribution of the neutron is seen for values of the momentum ratio smaller than about $\frac{1}{2}$, indicating that these events are consistent with being neutron spectator events. The conclusion from both these figures is that as the neutron-to-proton momentum ratio increases, the proton becomes more isotropically distributed about the beam and the neutron angular distribution

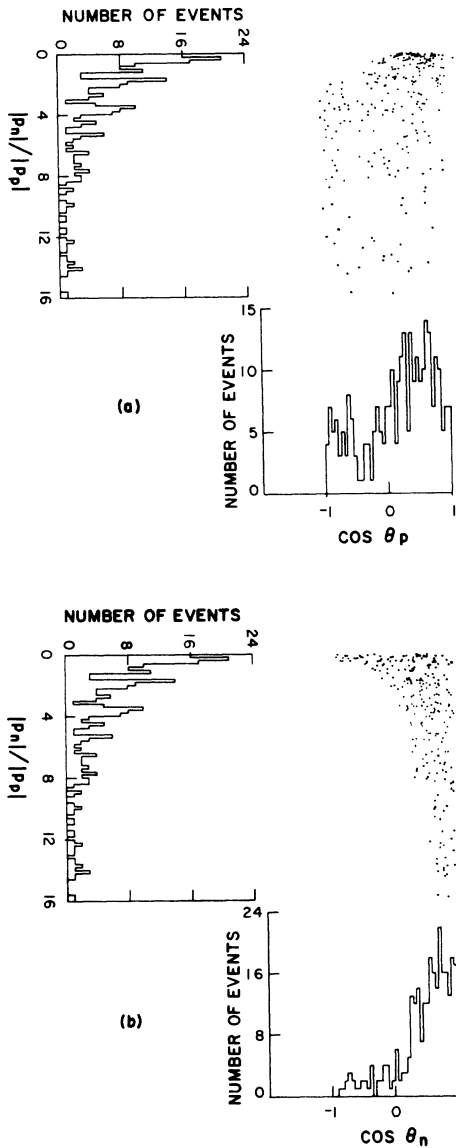


FIG. 5. A scatter diagram of the ratio of the magnitudes of fitted neutron and proton momenta for events fitting $K^-d \rightarrow \bar{K}^0\pi^-np$ versus (a) the angle between the proton and the incident particle, and (b) the angle between the neutron and the incident particle.

is more peaked in the direction of the beam.

We obtain an enriched sample of proton-spectator events by excluding events with the neutron momentum smaller than the proton momentum. Note that the prominent $\Delta^-(1236) \rightarrow n\pi^-$ signal in the selected sample is not apparent in the rejected sample, and we estimate that use of this selection criterion results in a loss of proton-spectator events from reaction (2.3) of less than 7%. The cross section obtained for reaction (2.3) is given in Table II and discussed further in Sec. IV.

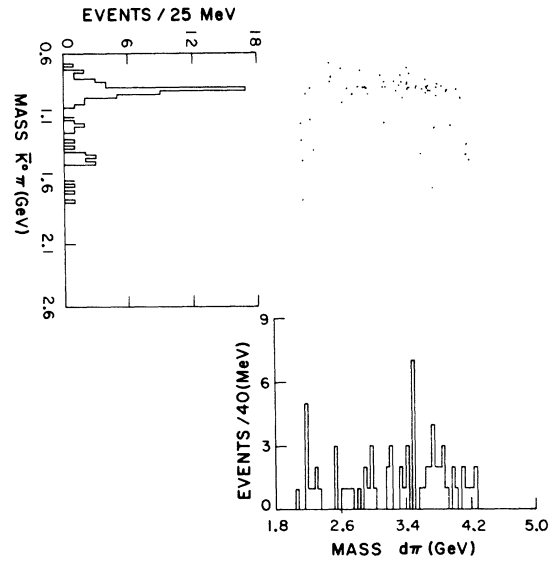


FIG. 6. Invariant mass of $(\bar{K}^0\pi^-)$ versus $(d\pi^-)$ for the reaction $K^-d \rightarrow \bar{K}^0\pi^-d$.

III. PROPERTIES OF THE COHERENT REACTION

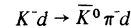


Figure 6 illustrates the strong coherent production of $\bar{K}^{*0}(890)$ and a suggestion of $\bar{K}^{*0}(1420)$ production in the quasi-two-body reactions

$$K^-d \rightarrow \bar{K}^{*0}(890)d, \quad (3.1)$$

$$K^-d \rightarrow \bar{K}^{*0}(1420)d. \quad (3.2)$$

The $d\pi^-$ invariant-mass projection of Fig. 6 shows a small signal at 2200 MeV, the " $d^*(2200)$," which could indicate a small contamination from the breakup reaction (1.1) since, as shown later, the $\Delta^-(1236)$ is produced strongly in the breakup channel and $M(d^*) \approx M(\Delta) + M(N)$. However, it is seen that the d^* signal is quite weak and no corrections have been made.

Because the deuteron has $I=0$, reaction (3.1) has been used to study the characteristics of ω exchange.^{9,10} However, the production amplitude for vector exchange processes vanishes in the forward direction, just where the deuteron has the largest probability of remaining intact, so that one does not expect a large cross section. To study the production and decay of the $\bar{K}^{*0}(890)$, we select events in the mass region $0.78 \text{ GeV} \leq M(\bar{K}^0\pi^-) \leq 1.2 \text{ GeV}$, which, from Fig. 7, is seen to include negligible background. The cross sections for the reactions (1.2) and (3.1), fully corrected for unobserved decay modes, are given in Table I. The distribution in four-momentum transfer to the deuteron for reaction (3.1) is shown in Fig. 8. The

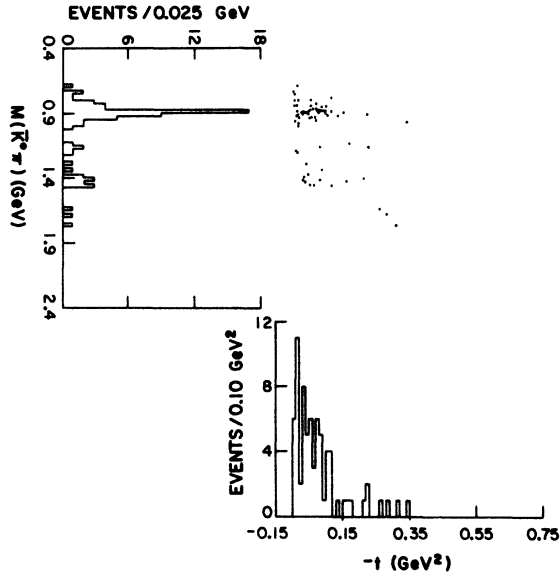


FIG. 7. Chew-Low plot for the reaction $K^-d \rightarrow \bar{K}^0\pi^-d$.

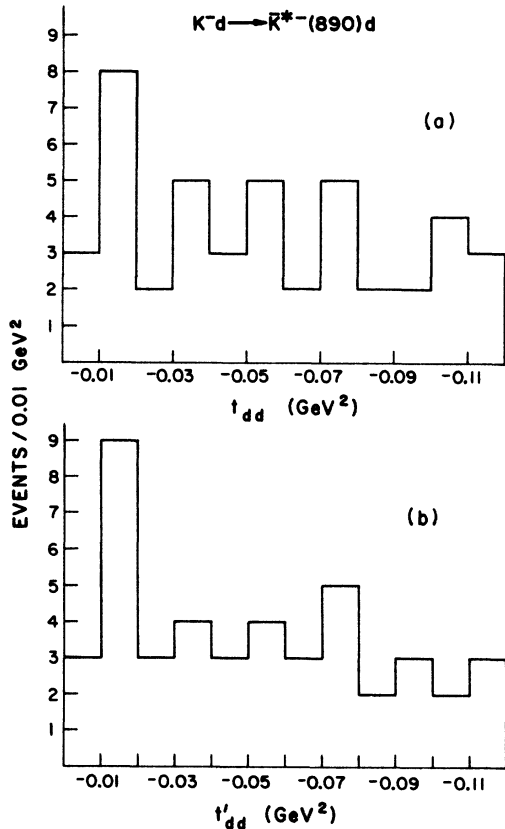


FIG. 8. (a) Four-momentum transfer t_{dd} distribution for the reaction $K^-d \rightarrow \bar{K}^*(890)\pi^-d$; (b) $t'_{dd} = (t - t_{\min})_{dd}$ for the same reaction.

deuteron form factor, of course, inhibits $\bar{K}^*(890)$ production at large four-momentum transfer.

The t -channel production mechanism for the coherent reaction (3.1) is conveniently discussed in terms of the density matrix for the $\bar{K}^*(890)$, expressed in the Gottfried-Jackson frame in which the production plane normal and the incident K^- direction form the y and z axes, respectively, as seen in the resonance rest frame. We also introduce a second reference frame to be used later, the helicity frame, also defined in the resonance rest system but using the production normal as the y axis and the resonance direction in the over-all c.m. system as the z axis. If the $\bar{K}^*(890)$ in reaction (3.1) is produced by the t -channel exchange of a single vector particle, then in the absence of absorptive effects the $\bar{K}^*(890)$ should be aligned with $m_x = \pm 1$ in the Jackson coordinate frame.

We have used the method of moments in order to determine the density-matrix elements for the $\bar{K}^*(890)$ decay in the Jackson and helicity frames, averaged over all four-momentum transfers. We obtain the values

$$\rho_{11}^{GJ} = 0.43 \pm 0.04,$$

$$\rho_{1-1}^{GJ} = 0.48 \pm 0.07,$$

$$\text{Re}\rho_{10}^{GJ} = 0.02 \pm 0.05.$$

These are in very good agreement with the expected values of 0.5, 0.5, and 0.0, respectively, associated with pure ω^0 exchange.

IV. THE FINAL STATE $\bar{K}^0\pi^-n(p_s)$

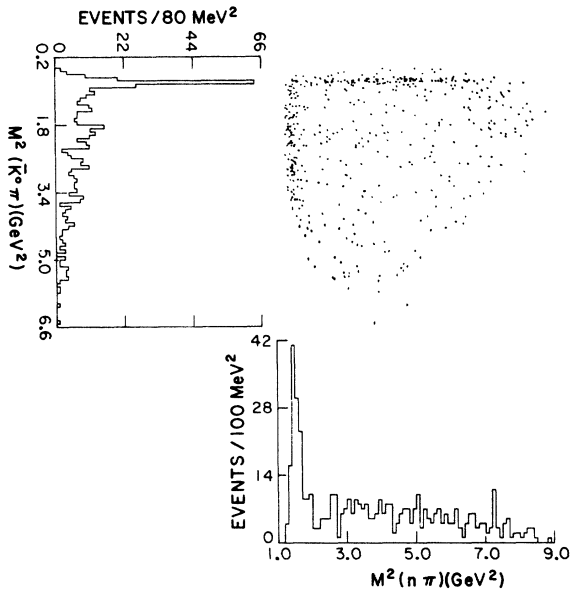
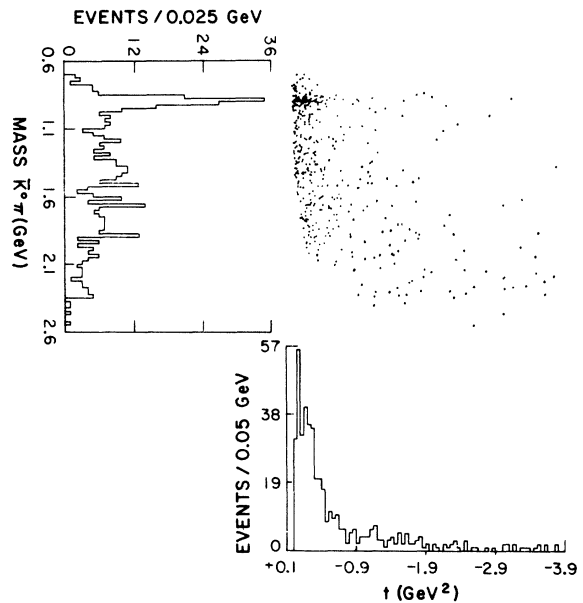
The procedures discussed in Sec. II B for selecting fits belonging to reaction (1.1) yielded a total of 540 accepted fits, including events where the proton produced a visible track as well as those where it did not. The cuts outlined in that same section, together with the requirement that the proton momentum be less than 300 MeV/c, reduced this number to 471 events consistent with the reaction

$$K^-d \rightarrow \bar{K}^0\pi^-n p_s. \quad (4.1)$$

From the neutron missing-mass peak of Fig. 4, we conclude that there is a 6% background contamination in the event sample ascribed to reaction (4.1), and the appropriate correction is included in the quoted cross section. The details of the cross section for this final state are summarized in Table II.¹¹

A. Resonance Production

The Dalitz plot for the $\bar{K}^0\pi^-n(p_s)$ final state is shown in Fig. 9. There is a pronounced cluster of

FIG. 9. Dalitz plot for the reaction $K^-d \rightarrow \bar{K}^0\pi^-np_s$.FIG. 10. Chew-Low plot for the reaction $K^-d \rightarrow \bar{K}^0\pi^-np_s$.

events corresponding to production of the $\bar{K}^{*-}(890)$ and of the $\Delta^-(1236)$, as well as a much weaker enhancement corresponding to $\bar{K}^{*-}(1420)$ resonance production. There is no evidence for interference between either \bar{K}^{*-} resonance and the $\Delta^-(1236)$, in agreement with the data at 4.5 GeV/c.¹² This situation contrasts with that at 3.5 GeV/c for the charge-symmetric reaction $K^+p \rightarrow K^0\pi^+p$, for which constructive interference in the crossover region of the $K^*(1420)$ and $\Delta(1236)$ resonance bands was seen. The effect may be energy-dependent.

The fractions of resonance production for $\bar{K}^{*-}(890)$, $\bar{K}^{*-}(1420)$, and $\Delta^-(1236)$ and the non-resonant $\bar{K}^0\pi^-n$ direct-channel contribution were determined by fitting the distribution of events over the Dalitz plot using the method of maximum likelihood.¹³ The small amount of $Y^{*0}(1520)$ production occurring in the \bar{K}^0n channel is ignored in making these fits. The resonance cross sections based on the results of this fit are given in Table II.

We define the events having $\bar{K}^0\pi^-$ effective mass in the range $0.82 \text{ GeV} \leq M(\bar{K}^0\pi^-) \leq 0.96 \text{ GeV}$ as representing the $\bar{K}^{*-}(890)$. To study the $\Delta^-(1236)$ characteristics, we use the mass band $1.12 \text{ GeV} \leq M(n\pi^-) \leq 1.34 \text{ GeV}$. The background included in the former mass selection is estimated to be less than 20% for the reaction

$$K^-n \rightarrow \bar{K}^{*-}(890)n. \quad (4.2)$$

In the case of the reaction

$$K^-n \rightarrow \bar{K}^0\Delta^-(1236), \quad (4.3)$$

the background is estimated to be smaller than 15%. In both cases, the background is ignored.

B. $K^*(890)$ Production and Decay

The peripheral nature of the \bar{K}^{*-} production can be seen in the Chew-Low plot of Fig. 10, where both the $\bar{K}^{*-}(890)$ and $\bar{K}^{*-}(1420)$ are produced at small squared four-momentum transfers, $|t|$, between the incident K^- and the resonance. The production differential cross section for the $\bar{K}^{*-}(890)$ is shown as a function of t in Fig. 11, where each event has been corrected for \bar{K}^0 escape loss.

The differential cross section is described well by an equation of the form $d\sigma/dt = Ae^{bt}$ away from the forward direction. A least-squares fit of this equation to the data gave a slope $b = 4.54 \pm 0.75 \text{ GeV}^{-2}$, where the fit extended over the region $-0.15 \text{ GeV}^2 \leq t \leq -0.60 \text{ GeV}^2$.

The data suggest that the differential cross section falls off in the forward direction, i.e., for $|t| < 0.05 \text{ GeV}^2$. Such a forward dip was also seen for the reaction $K^-p \rightarrow \bar{K}^{*-}(890)p$ at 5.5 GeV/c,^{1,14} and other momenta. However, in this latter reaction, corrections are generally needed for scanning losses associated with the recoil proton. In the present case, the forward dip is not indicative of a scanning loss, although to some extent the dip is associated with recombination of the neutron and proton to populate reaction (3.1).

The peripheral nature of $\bar{K}^{*-}(890)$ production arises from the t -channel exchange of mesons, of which π , ρ , and ω are the candidates usually con-

sidered.¹⁵ We have used the density-matrix formalism for the $\bar{K}^{*-}(890)$ decay to estimate the relative importance of pseudoscalar and vector ex-

change. The $\bar{K}^{*-}(890)$ decay angular distribution may be written in terms of the spin density matrix elements as follows:

$$W(\cos\theta, \phi) = \frac{3}{4\pi} [\rho_{00} \cos^2\theta + \frac{1}{2}(1 - \rho_{00}) \sin^2\theta - \rho_{1-1} \sin^2\theta \cos 2\phi - \sqrt{2} \operatorname{Re}\rho_{10} \sin 2\theta \cos\phi], \quad (4.4)$$

where θ and ϕ refer to the \bar{K}^0 from the $\bar{K}^{*-}(890)$ decay evaluated in the Jackson coordinate frame. We have used the method of moments in calculating the density matrix elements for the $\bar{K}^{*-}(890)$, and the results are given as a function of four-momentum transfer t to the $\bar{K}^{*-}(890)$ in Table III. For the same t intervals, we also show in Table III the $\bar{K}^{*-}(890)$ density matrix elements evaluated in the helicity frame. One notes that, even in the forwardmost bin of four-momentum transfer, the amount of pseudoscalar exchange is small, and with increasing $|t|$ the dominance of vector exchange becomes quite apparent. This same effect is well known for the reaction $K^-p \rightarrow \bar{K}^{*-}(890)p$.^{1,14}

Similar observations have already been made for the $K^-n \rightarrow \bar{K}^{*-}(890)n$ and $K^-p \rightarrow \bar{K}^{*-}(890)p$ reactions at 4.5 GeV/c.¹⁶ The curves shown in Fig. 11

are the predictions of the one-particle-exchange model with absorption.¹⁵ The calculation incorporates both π and ω exchange, and the couplings are those used in a similar calculation at 4.5 GeV/c.¹⁶ The shape of the predicted differential cross section is in reasonable agreement with the data, but the predicted cross section is considerably larger than that measured. The model provides a reasonable description of the density matrix elements, as previously observed at 4.5 GeV/c.

For completeness, we also include in Table III the density matrix element combinations $\sigma_{\pm} = \rho_{11} \pm \rho_{1-1}$ evaluated in both the helicity and the Gottfried-Jackson reference frames. The utility of these combinations rests in the fact that σ_{+} gives the fraction of the cross section occurring by natural-parity exchange [$P = (-1)^J$], while σ_{-} gives

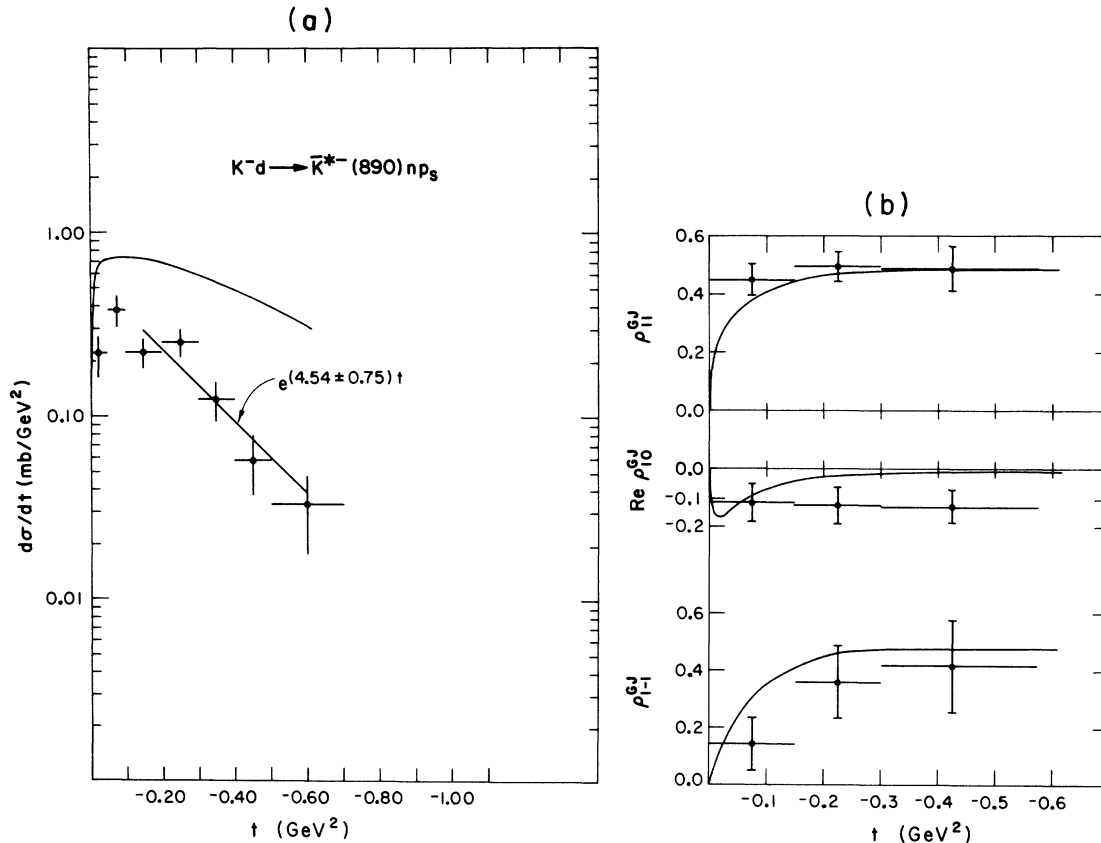


FIG. 11. (a) The distribution in four-momentum transfer and (b) the density-matrix elements for the reaction $K^-d \rightarrow \bar{K}^{*-}(890)np_s$. The curves are the predictions of an absorptive peripheral model with both π and ω exchange.

TABLE III. Density matrix elements for the $\bar{K}^{*-}(890)$ from reaction $K^-n \rightarrow \bar{K}^{*-}(890)n$.

$ t $ (GeV ²)	ρ_{11}^{GJ}	$\text{Re}\rho_{10}^{GJ}$	$\text{Re}\rho_{1-1}^{GJ}$	$\rho_{11}^{GJ} + \rho_{1+1}^{GJ}$	$\rho_{11}^{GJ} - \rho_{1-1}^{GJ}$	No. of events
$0 \leq t \leq 0.15$	0.45 ± 0.05	-0.12 ± 0.07	0.15 ± 0.09	0.60 ± 0.11	0.31 ± 0.11	40
$0.15 \leq t \leq 0.30$	0.50 ± 0.05	-0.13 ± 0.06	0.36 ± 0.13	0.86 ± 0.11	0.14 ± 0.11	34
$0.30 \leq t \leq 0.55$	0.49 ± 0.08	-0.13 ± 0.06	0.42 ± 0.16	0.90 ± 0.18	0.07 ± 0.18	20
$ t $ (GeV ²)	ρ_{11}^h	$\text{Re}\rho_{10}^h$	$\text{Re}\rho_{1-1}^h$	$\rho_{11}^h - \rho_{1-1}^h$	$\rho_{11}^h - \rho_{1-1}^h$	No. of events
$0 \leq t \leq 0.15$	0.32 ± 0.06	-0.0 ± 0.05	0.28 ± 0.09	0.60 ± 0.11	0.04 ± 0.11	40
$0.15 \leq t \leq 0.30$	0.39 ± 0.07	0.05 ± 0.07	0.47 ± 0.10	0.86 ± 0.12	-0.09 ± 0.12	34
$0.30 \leq t \leq 0.55$	0.45 ± 0.08	0.11 ± 0.06	0.45 ± 0.15	0.90 ± 0.17	-0.00 ± 0.17	20

the unnatural-parity [$P = (-1)^{J+1}$] fraction, for helicity-one K^* production.¹⁷ Closely similar results are observed at 5.5 GeV/c for the reaction $K^-p \rightarrow \bar{K}^{*-}(890)p$.¹⁴

C. Production and Decay of the $\Delta^-(1236)$

Figure 12 displays the differential cross section as a function of four-momentum transfer for the $\Delta^-(1236)$ produced in reaction (4.3). We have again fitted the differential cross section, excluding the

forward region (i.e., $|t| < 0.15$ GeV²), with an exponential function of t , and have determined the slope parameter to be $b = 4.28 \pm 0.66$ GeV⁻². The dip in the forward direction is again a genuine effect not arising from biases in the data. It has been suggested that this effect, seen in the production of the $\Delta^-(1236)$ in both KN and πN interactions, is due to the dominance of the s -channel single spin-flip amplitude.¹⁸

The allowed t -channel exchanges in this peripheral reaction are ρ and A_2 , and one notes that both

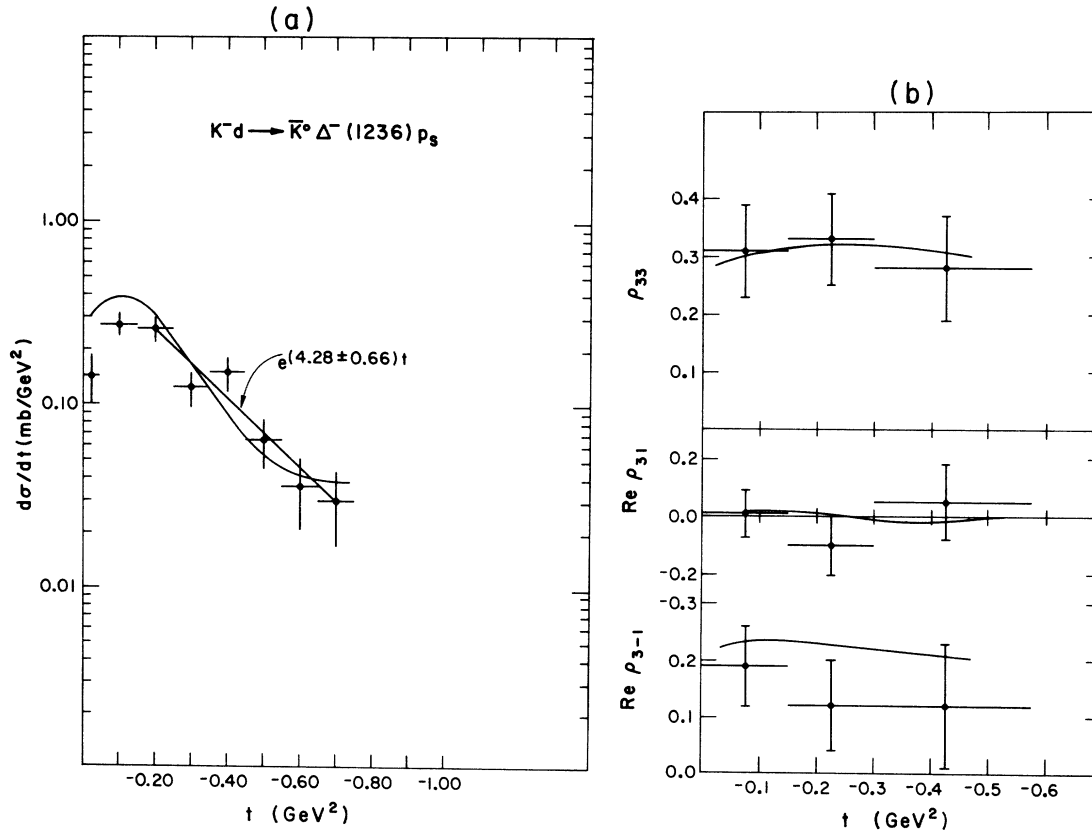


FIG. 12. (a) The distribution in four-momentum transfer and (b) the density matrix elements for the reaction $K^-d \rightarrow \Delta^-(1236)\bar{K}^0p_s$. The curves were obtained using a Reggeized absorption model with ρ and A_2 exchange.

TABLE IV. Density matrix elements for the $\Delta^-(1236)$ from reaction $K^-n \rightarrow \bar{K}^0\Delta^-(1236)$.

$ t $ range (GeV ²)	ρ_{33}^{GJ}	$\text{Re}\rho_{31}^{GJ}$	$\text{Re}\rho_{3-1}^{GJ}$	D^a
0 - 0.15	0.31 ± 0.08	0.01 ± 0.08	0.19 ± 0.07	0.023 ± 0.069
0.15 - 0.30	0.33 ± 0.08	-0.10 ± 0.10	0.12 ± 0.08	0.032 ± 0.072
0.30 - 0.55	0.28 ± 0.09	0.05 ± 0.13	0.12 ± 0.11	0.045 ± 0.074
Sakurai-Stodolsky prediction				
$\rho_{33} = 0.375$				
$\text{Re}\rho_{31} = 0.0$				
$\text{Re}\rho_{3-1} = 0.216$				

$$^a D = \rho_{33}\rho_{11} - (\text{Re}\rho_{31})^2 - (\text{Re}\rho_{3-1})^2.$$

of these natural-spin-parity mesons contribute to the same t -channel helicity states so that the $\Delta^-(1236)$ decay distribution does not allow one to distinguish between vector- and tensor-meson exchange. Indeed, the particular combination of density-matrix elements,

$$D = \rho_{33}(0.5 - \rho_{33}) - (\text{Re}\rho_{31})^2 - (\text{Re}\rho_{3-1})^2, \quad (4.5)$$

that tests for the exchange of a single trajectory¹⁹ is consistent with zero at all t values considered in Table IV. A violation of the condition that $D = 0$ would indicate the exchange of more than one trajectory, but, as pointed out in Ref. 19, satisfaction of this condition provides no information either way.

The density matrix elements of the $\Delta^-(1236)$ given in Table IV were again obtained using the method of moments. The ρ - γ ($M1$ -dominance) model²⁰ predictions are compared to the data in Table IV. The agreement is good, although we stress again that the same density-matrix elements would be obtained for either ρ or A_2 exchange.

The group of reactions producing a pseudoscalar meson in association with a $\Delta(1236)$ resonance can be discussed in terms of a very limited number of t -channel exchanges. Thus the reactions

$$\pi^+p \rightarrow \pi^0\Delta^{++} \quad (\rho \text{ exchange}), \quad (4.6a)$$

$$\pi^+p \rightarrow \eta^0\Delta^{++} \quad (A_2), \quad (4.6b)$$

$$K^+p \rightarrow K^0\Delta^{++} \quad (\rho + A_2), \quad (4.6c)$$

$$K^-n \rightarrow \bar{K}^0\Delta^- \quad (A_2 - \rho) \quad (4.6d)$$

afford a chance to test certain Regge-pole models.^{18,21} There are both similarities and differences between the above reactions. The values of the spin density matrix elements for the $\Delta(1236)$ are generally similar for these reactions and are not very sensitive to the particles exchanged. However, the differential cross sections show quite striking differences. The differential cross section for reaction (4.6a) is well known to show

the wrong-signature-nonsense dip near $t = -0.5$ GeV² associated with ρ exchange as well as other dips at higher momentum transfer. Reaction (4.6b) is known not to show any dip structure at $t = -0.5$ GeV² although a recent result suggests a dip near $t = -1.5$ GeV².²² Both reactions (4.6c) and (4.6d) are devoid of any striking features apart from the turnover of the differential cross section in the forward direction.

Given exact ρ - A_2 exchange degeneracy, the Regge model without absorption would predict equal cross sections for reactions (4.6c) and (4.6d).²³ However, the discrepancy already seen at lower energies is still apparent when comparing these reactions at 5 GeV/c and 5.5 GeV/c, respectively, and exceeds the small differences expected from the differing barycentric energies of the two experiments. We compare all available total cross section data for these two reactions in Fig. 13.²⁴ There is no evidence for better agreement at high-

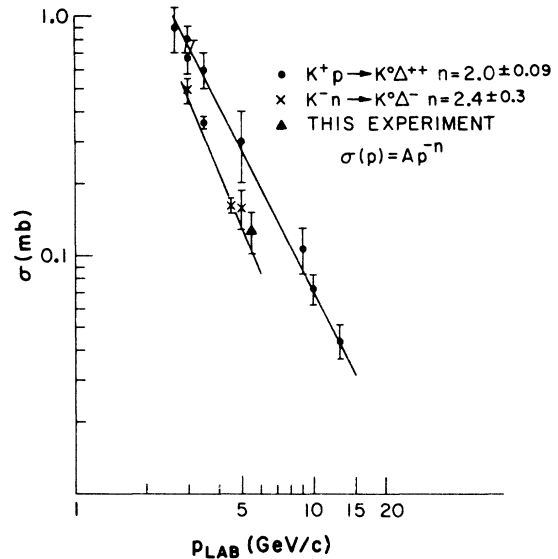


FIG. 13. The cross section for the reactions $K^+p \rightarrow K^0\Delta^{++}$ and $K^-n \rightarrow \bar{K}^0\Delta^-(1236)$ as a function of incident momentum.

TABLE V. Results of weak exchange-degeneracy S-wave absorption constant $C = 0.977$. Degrees of freedom = 385; $\chi^2 = 976$.

Vertex	Number of free parameters	Coupling γ	Value of γ
ρ Regge pole $\alpha = 0.5 + 0.9t$			
$N\bar{\Delta}$	3	$\gamma_{1/2\ 1/2}$	$(-3.07 - 20.05^a t)e^{1.62t}$
		$\gamma_{3/2\ 1/2}$	$(10.6 - 225.5^a t)e^{1.62t}$
		$\gamma_{-1/2\ 1/2}$	$(-28.3 - 135.7^a t)e^{1.62t}$
$K\bar{K}$ $\pi\pi$	1	$\gamma_{-3/2\ 1/2}$	75.1^a
		γ_{00}	-1.0^b
		γ_{00}	-2.40
A_2 Regge pole $\alpha = 0.5 \pm 0.9t$			
$N\bar{\Delta}$	3	$\gamma_{1/2\ 1/2}$	$(-1.01 + 13.01^a t)e^{-0.15t}$
		$\gamma_{3/2\ 1/2}$	$(24.98 - 278.5^a t)e^{-0.15t}$
		$\gamma_{-1/2\ 1/2}$	$(-17.45 + 202.3^a t)e^{-0.15t}$
$K\bar{K}$ $\eta\pi$	1	$\gamma_{-3/2\ 1/2}$	-2.24^a
		γ_{00}	-1.0^b
		γ_{00}	0.93

^a Parameters fixed by threshold constraints.

^b Parameters fixed by SU(3) constraint.

er momenta. This contrasts with the situation for the K^+n and K^+p charge-exchange reactions, where the two cross sections converge rapidly as the momentum increases from 3 to 12 GeV/c,²⁵ with close agreement achieved by 5.5 GeV/c.

The K^+p and K^+n reactions could differ as a result of the breaking of ρ - A_2 exchange degeneracy and also because of the differences in the initial- and final-state absorptions for these two reactions.²⁶ The extent of the ρ - A_2 exchange-degeneracy breaking may be estimated by noting that¹⁸

$$|\alpha_\rho(0) - \alpha_{A_2}(0)| \approx 0.15, \quad (4.7)$$

while the equality of the density matrix elements for the $\Delta(1236)$ produced from reactions (4.6) indicates a similar coupling for the ρ and A_2 . Since the density matrix elements are roughly the same and the difference in $\alpha(0)$ between the two trajectories is small, it seems unlikely that ρ - A_2 exchange-degeneracy breaking is accounting for all the observed difference between reactions (4.6c) and (4.6d).

Explaining the difference by absorption may be qualitatively correct since the K^- reaction is more absorptive than the K^+ , but the difference due to this effect should be less important with increasing energy. From 3 to 5 GeV/c, it is not clear from the data, even qualitatively, that the absorptions for the K^+ and K^- are becoming equal, for the differential cross sections are still widely separated in comparing the 5-GeV/c K^+ data and our 5.5-GeV/c data.

We have used a Reggeized absorptive model²⁷ to fit the data for reactions (4.6). In addition to the

t -channel exchange of ρ and A_2 Regge poles, the model includes the Regge-cut contribution for these poles through the strong (SCRAM) absorptive corrections to the initial and final states. We assume the weak form of exchange degeneracy in which the ρ and A_2 are represented by the trajectory function

$$\alpha(t) = 0.5 + 0.9t, \quad (4.8)$$

and the factorized residues are parametrized as shown in Table V. A total of twelve parameters were varied in fitting the available data for reactions (4.6).²⁸ These parameters, given in Table V, comprise eight coupling constants plus two exponential residue factors, and the strength of the absorption, and to allow for normalization difficulties one experiment in reaction (4.6a) is scaled.

We show the model predictions for the data of this experiment in Fig. 12 and see that the agreement with the data is good. The fit to the differential cross-section measurements for reactions (4.6a)-(4.6d) are shown in Figs. 14-17, respectively. The over-all χ^2 for the fit was 976 for 385 degrees of freedom, and the fitted values of the parameters are shown in Table V. In the case of reaction (4.6a), there is some difficulty in reproducing the dip and second maximum for the data below 5 GeV/c. The fit to the other three reactions is generally good, as it is also for the density matrices (not shown). In particular, the difference in size between the K^+p and K^-n reactions is well reproduced, as are the details of the differential cross section for the latter reaction.

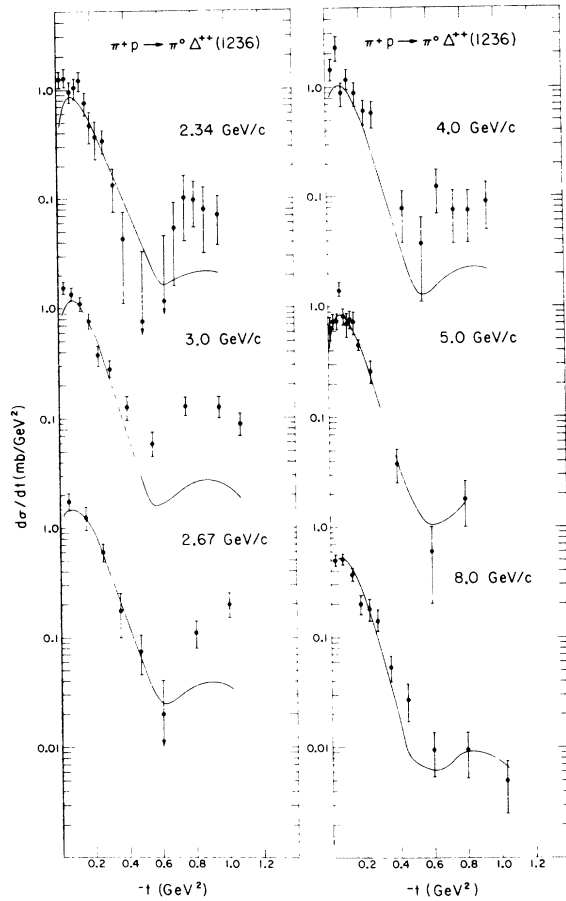


FIG. 14. Four-momentum-transfer distribution for the reaction $\pi^+p \rightarrow \pi^0\Delta^+(1236)$ at the indicated momenta. The curves were obtained from the Reggeized absorption model described in the text.

D. Generalized Veneziano Model Applied to $K^-n \rightarrow \bar{K}^0\pi^-n$

The process $K^-n \rightarrow \bar{K}^0\pi^-n$ is the charge-symmetric reaction to $K^+p \rightarrow K^0\pi^+p$ for which Chan Hong-Mo *et al.*²⁹ have attempted a description over a wide range of momentum using the generalized Veneziano model. Starting from twelve noncyclic and nonreflective B_5 graphs, we have reduced this to four graphs which do not include exotic subchannels. In Fig. 18, we show these four graphs and their dual diagrams. The Regge trajectories inserted between two external particles are also shown. These trajectories are the same as those used in Ref. 29, which also gives the details of the model briefly summarized here.

The relative weight of each diagram was determined by the following arguments:

(a) Non-exchange degeneracy of the Δ trajectory (lack of observation of a resonance having $J^P = \frac{5}{2}^-$) requires that diagrams (1) and (2) be added with

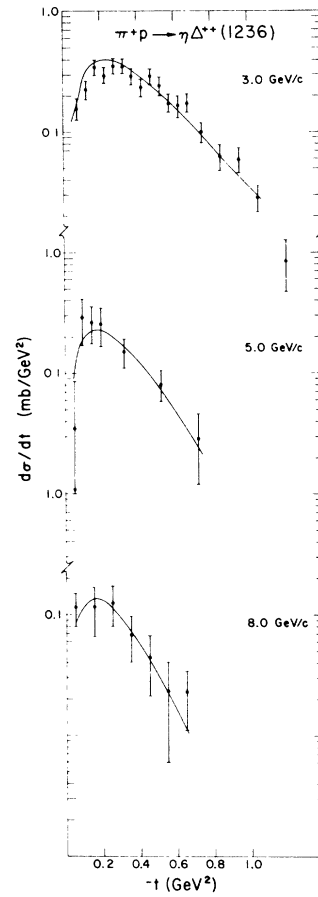


FIG. 15. Four-momentum-transfer distribution for the reaction $\pi^+p \rightarrow \eta\Delta^+(1236)$ at the indicated momenta. The curves represent a fit using a Reggeized absorption model.

equal weight.

(b) Non-exchange degeneracy of the N_α trajectory requires that diagrams (2) and (3) should have equal weight.

(c) Since the difference between diagrams (1) and (4) lies in the permutation of \bar{K}^0 and π^- , the exchange degeneracy of the K^*-K^{**} residues requires either diagram (1) or diagram (4). However, diagram (4) violates the Harari-Rosner rules; thus we eliminate diagram (4) from further consideration.

The reaction amplitude then becomes

$$A = K \sum_{i=1}^3 B_5^i, \quad (4.9)$$

where K is the kinematic factor, B_5^i is the five-point function of the i th diagram, and i runs over three diagrams. Since the first pole of each trajectory in all diagrams is either a vector meson or a p -wave resonance, we use the vector kinematic factor, $K = \epsilon_{\alpha\beta\gamma\delta} P_1^\alpha P_2^\beta P_3^\gamma P_4^\delta$, where the P_i 's

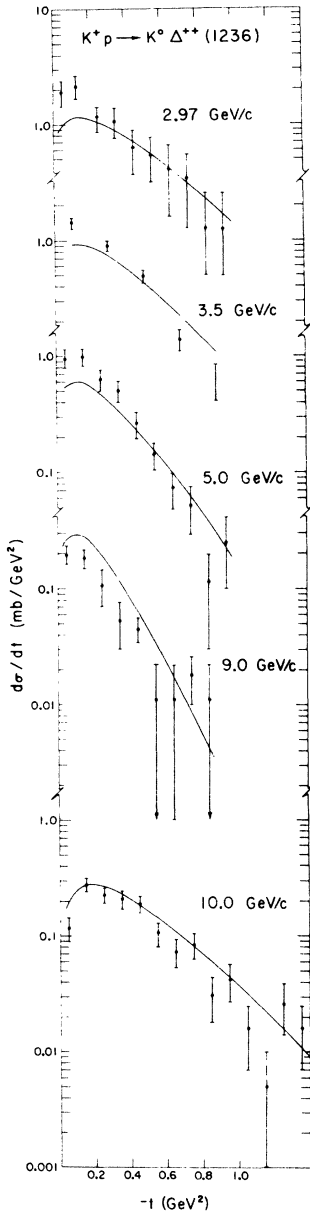


FIG. 16. Four-momentum-transfer distribution for the reaction $K^+p \rightarrow K^0\Delta^{++}(1236)$. The curves represent a fit using a Reggeized absorption model.

are the four-vectors of the four external particles and $\epsilon_{\alpha\beta\gamma\delta}$ is the totally antisymmetric tensor.

In order to compare the model prediction and data, we have generated phase-space events³⁰ weighted by the square of the above amplitude,³¹ according to a Monte Carlo method. In this way comparison between data and the predictions of all possible kinematic variables can be made.

The normalization of the model is given by Chan Hong-Mo *et al.* Accordingly, we have calculated

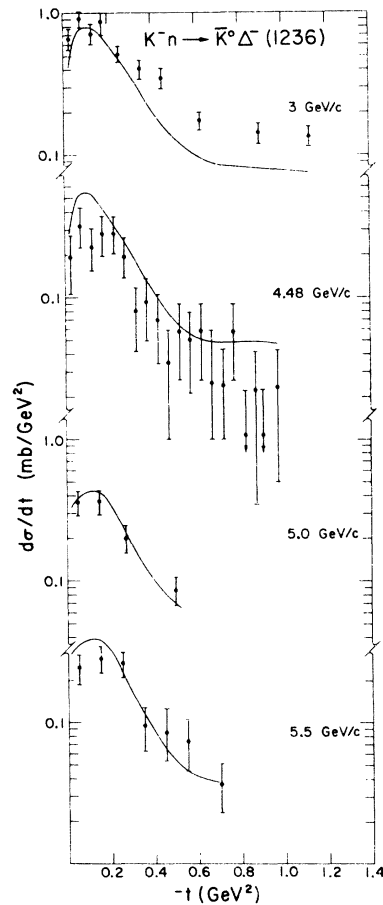


FIG. 17. Four-momentum-transfer distribution for the reaction $K^-n \rightarrow \bar{K}^0\Delta^-(1236)$. The curves represent a fit using a Reggeized absorption model.

the cross section for the reaction $K^-n \rightarrow \bar{K}^0\pi^-n$ at 5.5 GeV/c using their normalization constant, and find the cross section to be 900 μb , to be compared with the observed cross section of 450 μb . Because the predicted cross section is larger by a factor of 2, we have renormalized the model to the observed number of events in order to compare the model predictions for the distributions of kinematic variables to the experimental data.

Figure 19(a) shows the Van Hove plot together with the definition of the Van Hove angle ω . The connection between ω and the double-Regge diagram is also shown in Fig. 19(a). The distribution in the Van Hove angle is shown in Fig. 19(b), and the solid line is the prediction of the model normalized to the observed number of events. The production angular distributions and the longitudinal momentum distributions of the final-state particles in the over-all center-of-mass frame are shown in Figs. 20 and 21, respectively. They indicate that the agreement between the data and the

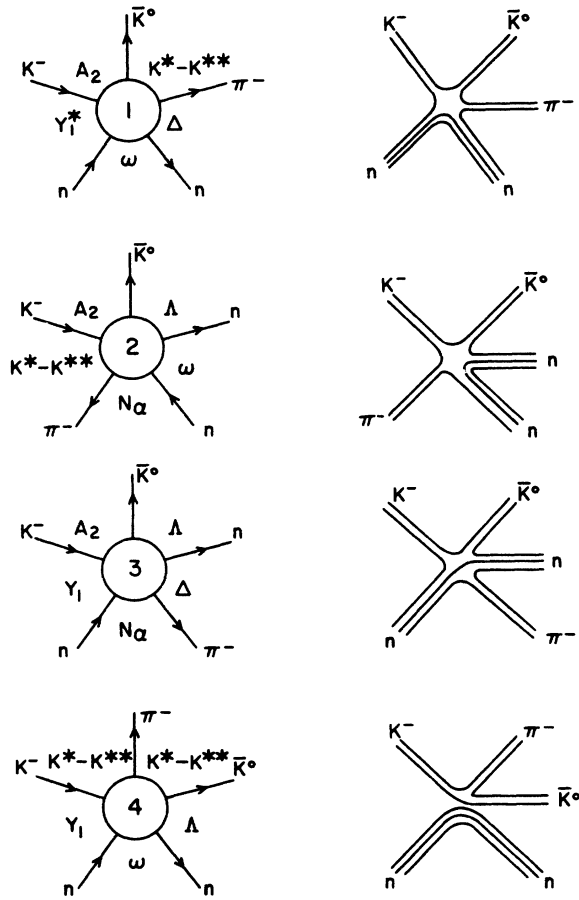


FIG. 18. B_5 graphs used in the Veneziano-model analysis of reaction $K^- n \rightarrow \bar{K}^0 \pi^- n$.

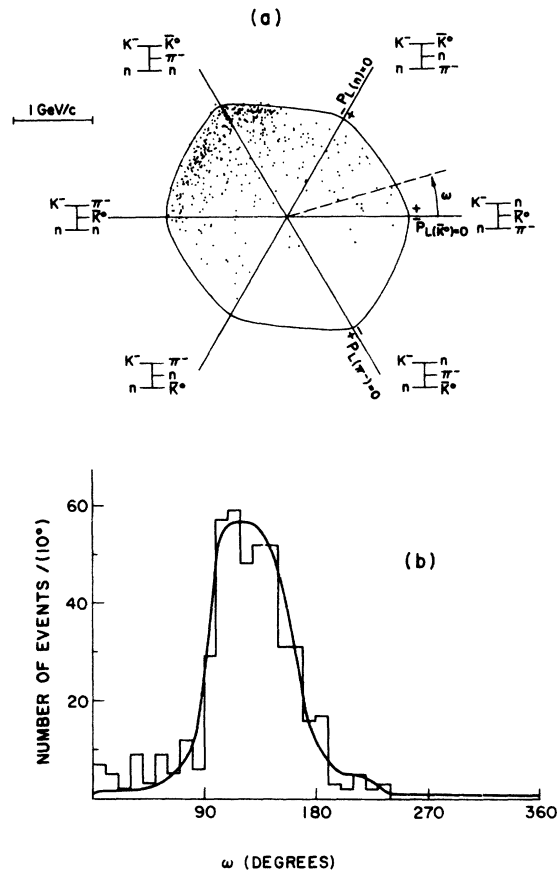


FIG. 19. (a) Van Hove plot for the reaction $K^- n \rightarrow \bar{K}^0 \pi^- n$; (b) distribution in the Van Hove angle with the Veneziano-model prediction shown.

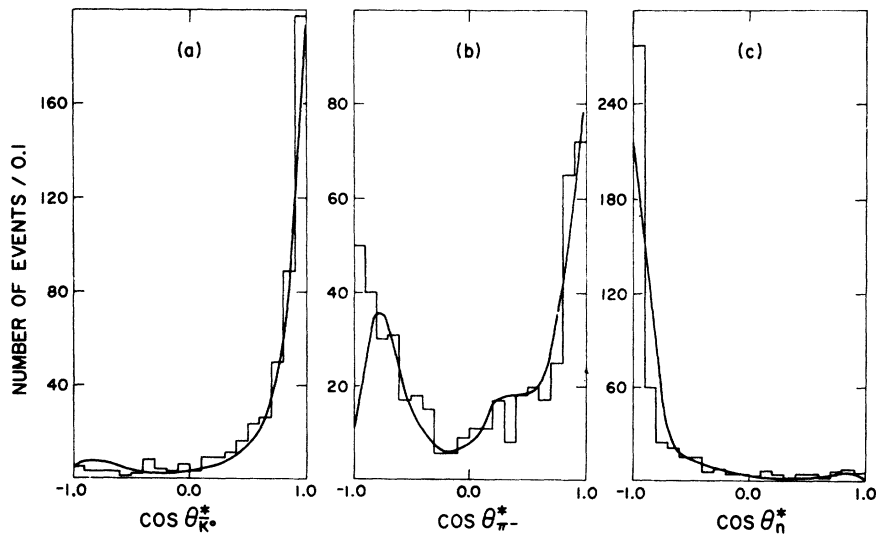


FIG. 20. The center-of-mass production angular distribution of particles in the reaction $K^- n \rightarrow \bar{K}^0 \pi^- n$ with the Veneziano-model predictions shown: (a) \bar{K}^0 , (b) π^- , (c) n .

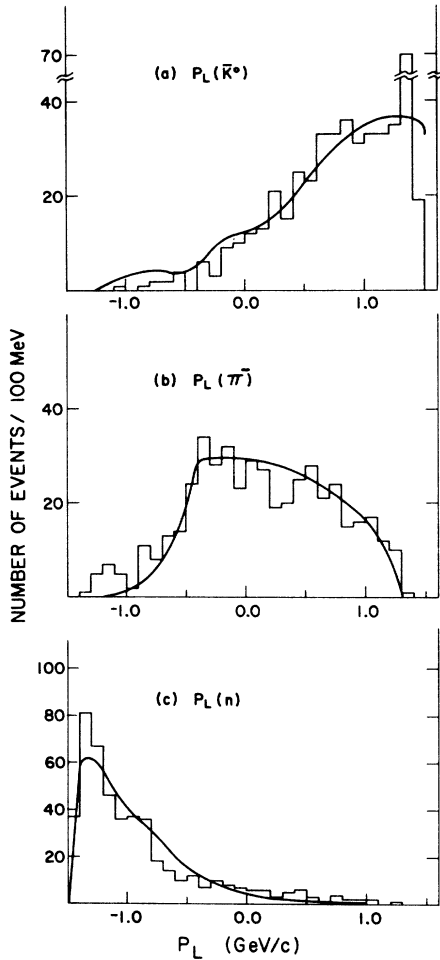


FIG. 21. The distribution in longitudinal momentum in the center-of-mass system for particles in the reaction $K^-n \rightarrow \bar{K}^0\pi^-n$. The Veneziano-model prediction is also shown: (a) \bar{K}^0 , (b) π^- , (c) n .

prediction is reasonable except that the distribution for the neutron is more sharply peaked than the model prediction. We attributed this discrepancy to the neglect of exchange of other particles, for example, pion exchange between the initial- and the final-state neutrons.

Figure 22 shows the two-body effective-mass distributions. For the subenergy distribution of the \bar{K}^0n system, the model predicts more $Y^*(1520)$ and $Y^*(1820)$ than is observed. The effective-mass distribution of the $\bar{K}^0\pi^-$ combination is well described by the model, while the model has difficulty in accommodating the Δ^- width in the $n\pi^-$ system, as noted in Ref. 29 for the K^+p analysis. The decay angular distributions of the $K^*(890)$ (not shown) are well described by the model. This is not surprising since, as is well known, the $K^*(890)$ in this reaction is dominated by ω exchange so that

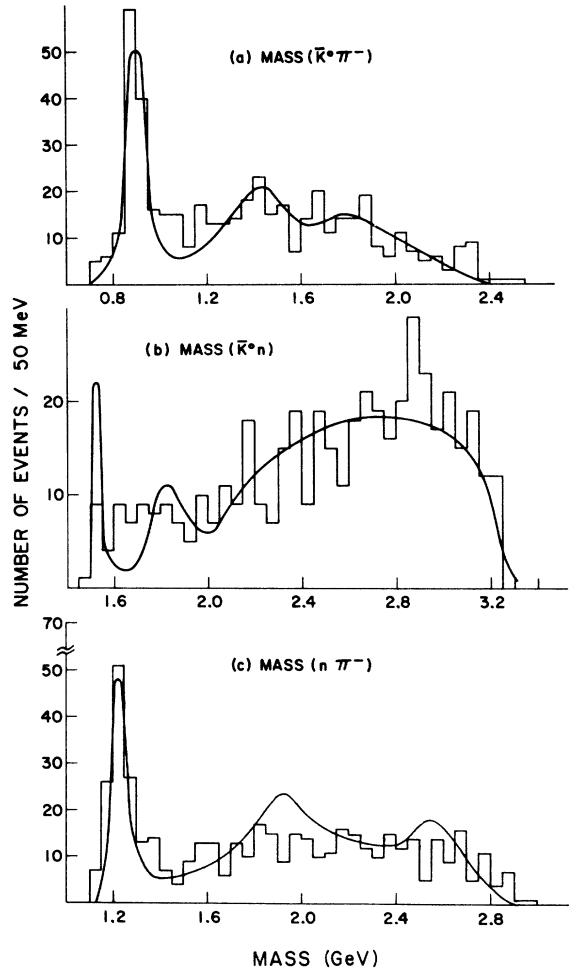


FIG. 22. Two-body effective-mass distributions for the reaction $K^-n \rightarrow \bar{K}^0\pi^-n$. The Veneziano-model predictions are shown: (a) $\bar{K}^0\pi^-$, (b) \bar{K}^0n , (c) $n\pi^-$.

the kinematic factor used in the model is guaranteed to reproduce these characteristics.

E. The Unfitted Channel

We also identify events for which the V^0 was shown to be a \bar{K}^0 but which gave no kinematic fit at the production vertex

$$K^-d \rightarrow \bar{K}^0\pi^-(p_s) + \text{missing neutrals}, \quad (4.10)$$

where the (p_s) denotes either a measured or an unseen proton. The mass of the $(\bar{K}^0\pi^-)$ system for these events is shown in Fig. 23. The $\bar{K}^*(890)$ is produced strongly with no other structure apparent. The spherical harmonic moments $\langle Y_L^0 \rangle$ in the Jackson frame of the $\bar{K}^0\pi^-$ system, computed from measured variables, are shown in Fig. 24. The

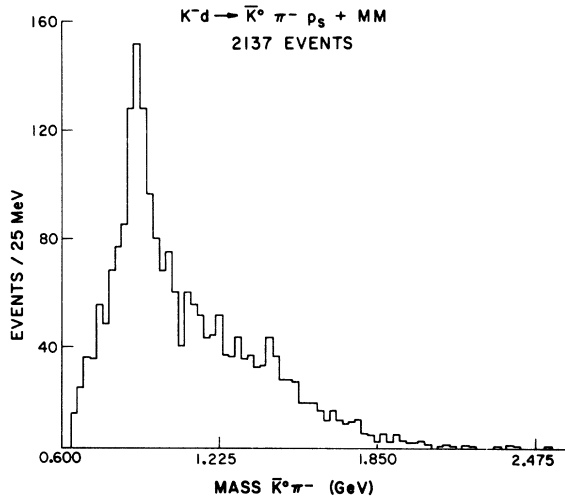


FIG. 23. $(\bar{K}^0\pi^-)$ effective mass using measured variables in the reaction $K^-d \rightarrow \bar{K}^0\pi^-p + MM$.

$\langle Y_2^0 \rangle$ moment in the $\bar{K}^{*0}(890)$ region shows neither a strong $\cos^2\theta$ nor a $\sin^2\theta$ characteristic.

V. CONCLUSIONS

We have studied the reactions $K^-d \rightarrow \bar{K}^0\pi^-d$ and $K^-n \rightarrow \bar{K}^0\pi^-n$ at a momentum of 5.5 GeV/c. A major contribution to the cross section of the coherent reaction comes from $\bar{K}^{*0}(890)$ production via an ω -exchange mechanism. The reaction $K^-n \rightarrow \bar{K}^0\pi^-n$ shows strong production of $\bar{K}^{*0}(890)$ and $\Delta^-(1236)$ resonances. The production and decay characteristics of the $\bar{K}^{*0}(890)$ are consistent with a vector-meson exchange mechanism. A good description of the $\Delta^-(1236)$ production and decay is achieved using a Reggeized absorption model. The

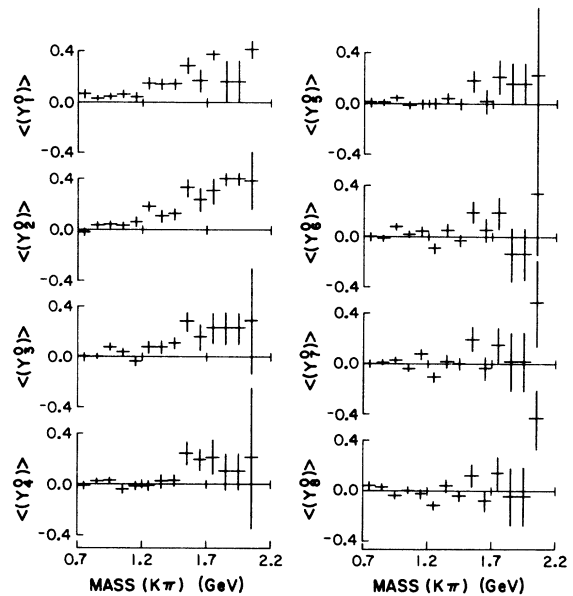


FIG. 24. $\langle Y_L^0 \rangle$ moments of the $(\bar{K}^0\pi^-)$ system in the reaction $K^-d \rightarrow \bar{K}^0\pi^-p_s + MM$.

reaction $K^-n \rightarrow \bar{K}^0\pi^-n$ is analyzed using a generalized Veneziano model (B_5) which provides a reasonable description of the data.

ACKNOWLEDGMENTS

It is a pleasure to recognize the help of the ZGS and 30-in. bubble chamber operating crews. We thank our scanning and measuring groups for their careful work. Thanks are due to E. Berger for advice and useful discussions.

†Work performed under the auspices of the U. S. Atomic Energy Commission and the National Science Foundation.

*ANL Predoctoral Fellow from the University of Kansas, Lawrence, Kansas. Presently at Louisiana State University, Baton Rouge, Louisiana. A dissertation based on this work has been submitted to the University of Kansas in partial fulfillment of the requirements for the Ph.D.

‡Visiting Scientist, Argonne National Laboratory, 1971-72.

¹F. Schweingruber *et al.*, Phys. Rev. **166**, 1317 (1968).

²B. Werner *et al.*, Phys. Rev. **188**, 2023 (1969);

B. Werner *et al.*, Nucl. Phys. **B23**, 37 (1970); Y. Cho *et al.*, Phys. Rev. D **3**, 1557 (1971); Y. Cho *et al.*, Phys. Letters **32B**, 409 (1970).

³K. W. J. Barnham *et al.*, Nucl. Phys. **B28**, 171 (1971).

⁴W. W. M. Allison *et al.*, Nucl. Instrum. Methods **84**, 129 (1970).

⁵The characteristics of the two event samples were verified to be consistent with one another.

⁶D. Johnson, Ph.D. thesis, University of Kansas, 1971 (unpublished).

⁷P. Fleury, *Methods in Sub-Nuclear Physics* (Gordon and Breach, New York, 1967), Vol. 2, p. 560.

⁸D. C. Brunt *et al.*, Phys. Rev. **187**, 1856 (1969).

⁹R. L. Eisner *et al.*, Phys. Letters **28B**, 356 (1968).

¹⁰D. Denegri *et al.*, Phys. Rev. Letters **20**, 1194 (1968).

¹¹An independent check of the cross section was made by normalizing the Hulthén spectator momentum distribution to the experimentally observed events in the region of proton momentum $80 \text{ MeV}/c \leq p_s \leq 300 \text{ MeV}/c$ for which the proton track was seen, in order to predict the total number of events we should observe. The

predicted number of events from this Hulthén normalization agreed well with the experimental total.

¹²R. L. Eisner *et al.*, Phys. Rev. 164, 1699 (1967).

¹³The program MINFUN was used to maximize the likelihood function for the Dalitz plot distribution, constructed using the Breit-Wigner amplitude appropriate to each resonance [J. D. Jackson, Nuovo Cimento 34, 1644 (1964)]. The fit assumes noninterfering resonances.

¹⁴R. Engelmann *et al.*, Phys. Rev. D 5, 2162 (1972).

¹⁵J. T. Donohue, Phys. Rev. 163, 1549 (1967).

¹⁶D. D. Carmony *et al.*, Nucl. Phys. B12, 9 (1969).

¹⁷J. P. Ader *et al.*, Nuovo Cimento 56A, 952 (1968).

¹⁸G. H. Renninger and K. V. L. Sarma, Phys. Rev. 178, 2201 (1967); M. Krammer and U. Maor, Nucl. Phys. B13, 651 (1969).

¹⁹G. Ringland and R. L. Thews, Phys. Rev. 170, 1569 (1968); A. Białas and A. Kotanski, Acta Phys. Polon. 30, 833 (1966).

²⁰L. Stodolsky and J. J. Sakurai, Phys. Rev. Letters 11, 90 (1963).

²¹R. D. Mathews, Nucl. Phys. B11, 339 (1969).

²²D. F. Grether and G. Gidal, Phys. Rev. Letters 26, 792 (1971).

²³K. W. Lai and J. Louie, Nucl. Phys. B19, 205 (1970); C. B. Chiu, Lawrence Radiation Laboratory report, 1971 (unpublished).

²⁴The total cross section is used since there is no significant backward peak in any of the experiments considered.

²⁵D. Cline *et al.*, Phys. Rev. Letters 23, 958 (1970).

²⁶C. Michael, Nucl. Phys. B13, 644 (1969).

²⁷The formalism of this model is described in G. C. Fox *et al.*, Phys. Rev. D 4, 2647 (1971). Further discussion of the absorption prescription and of the signature-factor parametrization is given in E. L. Berger and G. C. Fox, Nucl. Phys. B26, 1 (1971). SU(3) symmetry is assumed in this calculation to relate the following coupling constants: $\gamma_{\pi^+\eta A_2} = \frac{2}{3}\gamma_{K^+\bar{K}^0 A_2}$, $\gamma_{\pi^+\pi^0\rho} = 2\gamma_{K^+\bar{K}^0\rho}$. These exact relationships are allowed to be broken within certain limits.

²⁸The data used in this fit were obtained from the following sources:

$\pi^+p \rightarrow \pi^0\Delta^{++}$

2.34 GeV/c: A. Angelov *et al.*, JINR Report No. P1-4271, 1969 (unpublished).

2.67 GeV/c: G. Gidal *et al.*, Phys. Rev. Letters 23, 994 (1969).

3.50 GeV/c: G. Gidal *et al.*, LRL Report No. UCRL 18351 (unpublished).

4.0 GeV/c: ABBBHLM Collaboration, Phys. Rev. 138, 897 (1965).

5.0 GeV/c: D. J. Schotanus *et al.*, Nucl. Phys. B22, 45 (1970).

8.0 GeV/c: ABC Collaboration, Nucl. Phys. B8, 45 (1968).

$K^-n \rightarrow \bar{K}^0\Delta^-$

3.0 GeV/c: SABRE Collaboration. Private communication from A. M. Bakker, University of Amsterdam.

4.48 GeV/c: Reference 12.

5.00 GeV/c: B. J. Burdick *et al.*, Nucl. Phys. B41, 45 (1972).

5.5 GeV/c: This experiment.

$K^+p \rightarrow K^0\Delta^{++}$

2.97 GeV/c: Sallstrom *et al.*, Nuovo Cimento 49, 348 (1967).

2.97 GeV/c: M. Ferro-Luzzi *et al.*, Nuovo Cimento 36, 1101 (1967); 46, 539 (1966).

3.50 GeV/c: George *et al.*, Nuovo Cimento 46, 539 (1966).

5.00 GeV/c: George *et al.*, Nuovo Cimento 46, 539 (1966).

9.0 GeV/c: V. G. Lind *et al.*, Nucl. Phys. B14, 1 (1969).

10.0 GeV/c: K. W. J. Barnham *et al.*, Nucl. Phys. B28, 171 (1971).

12.70 GeV/c: B. Forman *et al.*, Nucl. Phys. B8, 333 (1968).

$\pi^+p \rightarrow \eta\Delta^{++}$

3.0 GeV/c: Reference 22.

5.0 GeV/c: D. J. Schotanus *et al.*, Nucl. Phys. B25, 109 (1971).

8.0 GeV/c: ABC Collaboration, Nucl. Phys. B8, 45 (1968).

²⁹Chan Hong-Mo *et al.*, Nucl. Phys. B19, 173 (1970).

³⁰The Fermi motion of the neutron target in the deuteron was taken into account.

³¹For the numerical evaluation of the five-point function, see J. F. L. Hopkinson, Daresbury Report No. DNPL/P 21, 1969 (unpublished).